



Abundances of siderophile elements in H-chondrite metal grains: implications for the origin of metal in unequilibrated ordinary chondrites

Guillaume Florin, Olivier Alard, Béatrice Luais, Tracy Rushmer

► To cite this version:

Guillaume Florin, Olivier Alard, Béatrice Luais, Tracy Rushmer. Abundances of siderophile elements in H-chondrite metal grains: implications for the origin of metal in unequilibrated ordinary chondrites. *Geochimica et Cosmochimica Acta*, 2022, 10.1016/j.gca.2022.11.014 . hal-03866321

HAL Id: hal-03866321

<https://hal.science/hal-03866321>

Submitted on 22 Nov 2022

HAL is a multi-disciplinary open access archive for the deposit and dissemination of scientific research documents, whether they are published or not. The documents may come from teaching and research institutions in France or abroad, or from public or private research centers.

L'archive ouverte pluridisciplinaire **HAL**, est destinée au dépôt et à la diffusion de documents scientifiques de niveau recherche, publiés ou non, émanant des établissements d'enseignement et de recherche français ou étrangers, des laboratoires publics ou privés.



Distributed under a Creative Commons Attribution - NonCommercial - NoDerivatives 4.0 International License

Abundances of siderophile elements in H-chondrite metal grains: implications for the origin of metal in unequilibrated ordinary chondrites

Guillaume Florin, Olivier Alard, Béatrice Luais, Tracy Rushmer

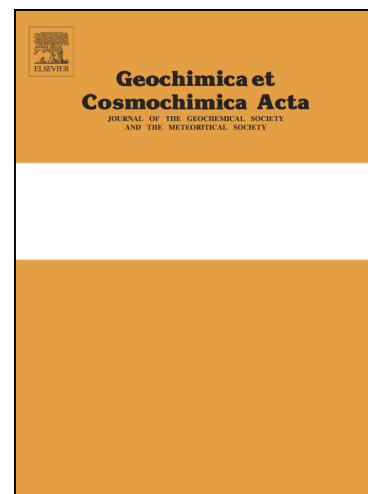
PII: S0016-7037(22)00621-4
DOI: <https://doi.org/10.1016/j.gca.2022.11.014>
Reference: GCA 12872

To appear in: *Geochimica et Cosmochimica Acta*

Received Date: 26 June 2022
Revised Date: 21 October 2022
Accepted Date: 14 November 2022

Please cite this article as: Florin, G., Alard, O., Luais, B., Rushmer, T., Abundances of siderophile elements in H-chondrite metal grains: implications for the origin of metal in unequilibrated ordinary chondrites, *Geochimica et Cosmochimica Acta* (2022), doi: <https://doi.org/10.1016/j.gca.2022.11.014>

This is a PDF file of an article that has undergone enhancements after acceptance, such as the addition of a cover page and metadata, and formatting for readability, but it is not yet the definitive version of record. This version will undergo additional copyediting, typesetting and review before it is published in its final form, but we are providing this version to give early visibility of the article. Please note that, during the production process, errors may be discovered which could affect the content, and all legal disclaimers that apply to the journal pertain.



Abundances of siderophile elements in H-chondrite metal grains: implications for the origin of metal in unequilibrated ordinary chondrites

Guillaume Florin^{a,b*}, Olivier Alard^{a,c}, Béatrice Luais^b, Tracy Rushmer^a

^a: Department of Earth and Planetary Sciences, Macquarie University, NSW 2109, Australia

^b: Université de Lorraine, CNRS, CRPG, F-54000 Nancy, France

^c: Géosciences Montpellier, UMR 5243, CNRS & Université Montpellier, 34095 Montpellier, France.

*: Corresponding author g.florin@fu-berlin.de

Present address: Freie Universität Berlin, Institute of Geological Sciences, 12249 Berlin, Germany

Abstract

Understanding the evolution of metal in the protoplanetary disk is necessary to constrain the first steps of metal-silicate formation and the early stages of the evolution of the protoplanetary disk. We measured the siderophile elemental compositions (PGE, Ni, Co, Fe, Cu, Ga, Ge) of individual metal grains in H ordinary chondrites by laser ablation inductively coupled plasma mass spectrometry to investigate their formation. We analyzed unequilibrated ordinary chondrites (H3) to constrain processes affecting the metal before accretion, and inferred the effects of metamorphism by comparing their elemental compositions to those of equilibrated chondrites (H4–H6). Our results highlight large variations of refractory (Re, Os, W, Ir, Ru, Mo, Pt) and moderately volatile siderophile element (Pd, Au, Ga, Ge) concentrations among metal grains in H3 samples that permit to classify them according to their Ge/Ir ratios and HSE contents. These intergrain variations are progressively homogenized in H4–H6 samples due to their increasing

degrees of metamorphism. To constrain the origin of the metal, we modeled its evolution during melting and crystallization. Our melting model of a single metallic precursor containing 1.5 wt.% C and up to 12 wt.% S reproduces well the observed range of siderophile element compositions in the metal. Metal grains show a range of W, Mo, and Ga compositions that we interpret to reflect various local (grain-scale) oxidation states during the melting event(s) due to the heterogeneous distribution of various oxidizing components within the precursors. The very similar HSE compositions of H and L/LL metal grains suggests that the variations of bulk metal abundance and HSE concentrations observed among the different classes of ordinary chondrites (H, L, LL) result from the heterogeneous physical distribution of a relatively chemically homogeneous metal component among OC parent bodies, and not from a chemical (*sensu lato*) gradient between H and LL chondrites.

Keywords: Partial melting, metal precursor, ordinary chondrites, siderophile elements, Germanium, Fe-Ni alloy

1 Introduction

Chondrites are undifferentiated primitive objects comprising a mixture of components with various compositions and textures that represent their diverse origins and formation processes. These components include chondrules, metal, sulfides, refractory inclusions, and fine-grained matrix. Metal and chondrules are chemically closely related, and understanding their formation in primitive chondrites is of primary importance to constraining the early evolution of the protoplanetary disk. Several processes can lead to metal formation, which vary among chondrite groups: (1) direct condensation from the solar nebula (Newsom and Drake, 1979) or an impact plume (Weyrauch et al. 2019); (2) reduction of iron from silicates (Kong and Ebihara, 1997) due to interaction with carbon (Connolly et al., 2001; Lauretta et al., 2001) or the nebular gas (Zanda et al., 1994); (3) desulfurization of sulfides due to evaporation (Cohen and Hewins, 2004); or (4) vapor recondensation following chondrule evaporation (Connolly et al., 2001).

Among ordinary chondrites (OCs), H chondrites are the most reduced, containing in average 8.4 vol. % metal (Krot et al., 2014). Both sub- and super-solar Co/Ni values are observed in metal in different H chondrites, precluding the possibility that the metal formed by condensation (Kong and Ebihara, 1997). In contrast, the similarity of the

metal-silicate partitioning coefficients of siderophile elements measured in OCs (Kong and Ebihara, 1997) to those in measured melting experiments (Brenan and McDonough, 2009) suggests metal formation by the reduction of FeO from silicate precursors during chondrule and chondritic metal formation (Kong and Ebihara, 1997). Despite this apparent consistency, recent high-precision *in-situ* laser ablation inductively coupled plasma mass spectrometry (LA-ICP-MS) measurements highlight large variations in highly siderophile element (HSE) concentrations from one metal grain to another within the same sample (Campbell and Humayun, 2003; Okabayashi et al., 2019). Additionally, the lack of correlation between the concentrations of refractory HSEs (Re, Os, Ir, Ru, Pt) and moderately refractory siderophile elements (Pd, Au) (Campbell and Humayun, 2003), as well as the solar Fe/Si ratio (Palme et al., 2014) makes it difficult to explain metal formation in H chondrites exclusively by the reduction of FeO in silicates.

Horan et al. (2009) related these variations in HSE composition to metal grain size, showing that small grains are enriched in HSEs compared to larger ones. They demonstrated that metal formation cannot have resulted from melting at high sulfur contents (~25 wt.%). Although they did not reproduce solar Co/Ni ratios, they argued that the high HSE contents of small grains resulted from their condensation at high temperature, whereas the low HSE contents of large grains reflected their condensation at lower temperatures. Thus, the large range of compositions observed might result from these two types of metal forming separately and subsequently mixing without equilibrating (Grossman and Wasson, 1985; Horan et al., 2009). This argument is supported by the high and variable Pd contents relative to Fe in the HSE-rich metal phase, which can only result from condensation at high to moderate temperatures and high pressures ($>10^{-4}$ bar); otherwise, Pd and Fe would condense at the same temperature and thus at a constant Pd/Fe ratio in the metal. Alternatively, Campbell and Humayun (2003) suggested that the large variability among metal compositions more likely results from the incomplete homogenization of HSEs in the metal of ordinary chondrites. A third possibility is the production of metal by troilite desulfurization (Hewins et al., 1997), as observed in the experiments of McCoy et al. (1999). Finally, recent *in-situ* measurements by Okabayashi et al. (2019) demonstrate that the variable metal compositions in L and LL OCs result from the melting and crystallization of metal precursors. In summary, despite multiple theories seeking to explain the metal diversity in ordinary chondrites in recent decades, no consensus exists. Therefore, a careful investigation of metal compositions in OCs is needed.

Here, we performed LA-ICP-MS measurements of HSE and MSE concentrations in metal phases associated with both unequilibrated (UOC, H3) and equilibrated H chondrites (EOC, H4–H6). We analyzed individual metal grains inside and outside chondrules. These primitive meteorites were chosen to constrain the formation of metallic

phases in the solar nebula and provide new constraints on metal precursors. We use our measurements of EOC metal to illustrate the effect of metamorphism on metal compositions and thus demonstrate the lack of metamorphic overprinting in our H3 samples. We then compare our data on H chondrites to data for L and LL chondrites (Okabayashi et al., 2019) to infer the formation and distribution of metal in the protoplanetary disk.

2 Methods

2.1. Sample selection

Ordinary chondrites were chosen according to the classification of Van Schmus and Wood (1967). To constrain metal formation in H ordinary chondrites, we selected three unequilibrated H3 chondrites: Asuka 881236 (H3.1; A-881236.57, National Institute of Polar Research, Tokyo), Sharps (H3.4; USNM 640, Smithsonian National Museum of Natural History, Washington, D.C.), and Dhajala (H3.8; USNM 5832, Smithsonian). To assess the effects of the compositional evolution of metal during metamorphism, we selected five equilibrated H ordinary chondrites: Ste. Marguerite (H4; MNHN 3290, Museum National d'Histoire Naturel, Paris), Allegan (H5; USNM 215, Smithsonian), Portales Valley (H6; USNM 6975, Smithsonian), Kernouvé (H6; Smithsonian), and Guareña (H6; Museo Nacional de Ciencias Naturales, Madrid).

2.2. Analytical Procedures

Samples were cut using a diamond saw, mounted in resin, and processed as polished sections. Samples were first examined by optical microscopy under reflected light, then with a Zeiss EVO MA15 tungsten-filament scanning electron microscope at Macquarie University, Sydney, Australia. Elemental (K α) X-ray maps were acquired using an Oxford Instruments 20 mm² X-max silicon-drift energy dispersive spectrometer, and the data were processed using Oxford Instruments AZtec acquisition software v3.2. From these maps, we selected grains of interest outside, at the edges of, and within chondrules for siderophile elemental analysis by LA-ICP-MS. Due to the small sizes of the

metal grains in chondrules (*e.g.* between 40 and 10 μm) most of them cannot be analyzed, and we obtained fewer analyses within chondrules than in the interchondrule matrix.

In-situ analyses were conducted using a LA-ICP-MS comprising a G2 photon machine 193-nm HelEx Cell laser ablation peripheral connected to a 7500 Agilent ICP-MS. The gas injected into the laser chamber was a mixture of helium and nitrogen, and the laser fluence was $\sim 7 \text{ J/cm}^2$. Static spot analyses were performed using a 30–80- μm spot size depending on size of the grain being analyzed. Each measurement comprised 160 s of blank analysis, 60 s of integrated signal analyses, and then 60 s of washout. Each analytical spot was ablated by 300 laser pulses at 5 Hz. The isotopes ^{34}S , ^{57}Fe , ^{59}Co , ^{60}Ni , ^{61}Ni , ^{63}Cu , ^{65}Cu , ^{66}Zn , ^{68}Zn , ^{69}Ga , ^{74}Ge , ^{95}Mo , ^{99}Ru , ^{101}Ru , ^{103}Rh , ^{105}Pd , ^{106}Pd , ^{108}Pd , ^{182}W , ^{185}Re , ^{192}Os , ^{193}Ir , ^{195}Pt , and ^{197}Au were measured in all analyses. These elements were selected to represent a range of volatilities, from refractory elements (Re, Os, Ir, Pt, Ru, Rh, Mo, W) to moderately volatile elements (MVEs; Au, Ga, Ge), and chemical behaviors, ranging from highly siderophile (Re, Os, Ir, Pt, Ru, Rh, Pd, Au) to moderately siderophile (Ni, Co, Fe, Cu, Ga, Ge) and chalcophile elements (*e.g.* Cu). Formation of argide poly atomic interferences such as $^{61}\text{Ni}^{40}\text{Ar}$ on ^{101}Ru or $^{63}\text{Cu}^{40}\text{Ar}$ on ^{103}Rh are checked by comparing counts obtained on ^{105}Pd ($^{65}\text{Cu}^{40}\text{Ar}$), ^{106}Pd ($^{66}\text{Zn}^{40}\text{Ar}$) and ^{108}Pd ($^{68}\text{Zn}^{40}\text{Ar}$) and on ^{99}Ru ($^{59}\text{Co}^{40}\text{Ar}$) against ^{101}Ru ($^{61}\text{Ni}^{40}\text{Ar}$). If these ratios are significantly different than the accepted natural ratio (*i.e.*, outside of uncertainties), then correction are applied accordingly. Given the ICP-MS setting, the low isotopic abundance of ^{61}Ni ($\approx 1.14\%$), and the low content of Cu in the metal and sulfide phases investigated, no correction was necessary. Calibration standards were run five times during each analytical session: PGE-A (a HSE-rich NiS bead; Alard et al., 2011) for Os, Ir, Ru, Pt, Rh, Co Pd, Au, and Cu; and Filomena (northern Chile, a IIAB iron meteorite commonly used for LA-ICP-MS analyses; see Walker et al., 2008 and references therein) for Re, W, Mo, Ni, Ga, and Ge (Appendix Table A1). Data were validated by comparing our analyses of the secondary standards Hoba (IVB iron meteorite) and NIST (National Institute of Standards and Technology) standard reference material 1158 with literature data (Walker et al., 2008). We report typical mean errors calculated as the propagated mean error compared to mean secondary standard analysis and reported in %: 31% (Re), 44% (Os), 44% (W), 20% (Ir), 17% (Ru), 21% (Mo), 10% (Pt), 15% (Rh), 9% (Ni), 3% (Co), 18% (Pd), 12% (Au), 13% (Cu), 8% (Ga), and 4% (Ge). The reproducibility of standard compositions is reported in appendix Table A2. All measured concentrations are calibrated with ^{57}Fe , ^{60}Ni , and ^{34}S as internal standards using sum normalization for Fe-Ni alloy (^{57}Fe , ^{60}Ni) and sulfides (^{34}S). Uncertainties are given as 1SD when it refers individual grains and to reflect the compositional variability as %RSD for mean values.

3 Results

3.1. Petrographic characteristics of metal grains

The petrographic characteristics of metal grains in the studied H chondrites are summarized in Fig. 1. The distribution of metal grains evolved with increasing degree of metamorphism. In H3 chondrites, metal grains are variously sized (from 10 μ m to \approx 3mm) and mostly very angular to sub-rounded, both inside and outside of chondrules (Fig. 1A–D). With increasing degree of metamorphism, small metal grains disappeared and tend to become more rounded (Fig. 1E–J). Small grains are notably more circular in H6 compared to H3 chondrites (Fig. 1). Finally, metal occurs in large veins in Portales Valley, and the surrounding clasts include silicates, large sulfides (>50 μ m), and disseminated metal grains (Fig. 1). Our observations are consistent with shape and circularity measurements reported by Guignard and Toplis (2015).

3.2. Compositions of metal phases

In-situ analyses of metal grains are presented in Fig. 2 and mean values in Table 1 (full data are available in appendix Table A3). Fe-Ni metal grain compositions are classified as Ni-rich taenite or Ni-poor kamacite. The Ni and Co concentrations in kamacite and taenite were found to be consistent with previously reported bulk (Kong and Ebihara, 1997) and in-situ kamacite data (Campbell and Humayun, 2003) for both UOCs and EOCs (Fig. 2). Specifically, taenite is enriched in Ni (38 wt.% \pm 25% relative standard deviation, RSD) and depleted in Co (0.18 wt.% \pm 33% RSD) compared to kamacite (6.1 wt.% Ni \pm 25% RSD; 0.41 wt.% Co \pm 22% RSD) and the bulk metal (Fig. 2). In some cases, phases with intermediate compositions (10–25 wt.% Ni) were analyzed; these are most likely plessite, a fine-grained mixture of kamacite and taenite (Gilmour and Herd, 2020).

Normalizing the mean elemental contents of metal in the H3–H6 chondrites to CI chondrites (Fig. 2) reveals superchondritic Re to Au and Ge compositions that are up to one order of magnitude higher than CI values (Lodders et al., 2009). In detail, CI-normalized kamacite mean elemental values show the same overall trend regardless of

metamorphic grade: a flat trend for refractory elements Re to Pd (*e.g.* $\text{Re}_{\text{Cl}} = 8.7$, $\text{Os}_{\text{Cl}} = 5.5$, $\text{Pt}_{\text{Cl}} = 6.2$, and $\text{Pd}_{\text{Cl}} = 5.1$, where the subscript 'Cl' indicates values normalized to CI chondrites) and relative depletion in the most volatile siderophile elements Au, Cu, Ga, and Ge ($\text{Au}_{\text{Cl}} = 4.2$, $\text{Cu}_{\text{Cl}} = 0.70$, $\text{Ga}_{\text{Cl}} = 0.69$, $\text{Ge}_{\text{Cl}} = 1.8$; Au and Cu also being chalcophile), with Ni, Pd, Au, Cu, and Ga also being depleted compared to the bulk metal data of Kong and Ebihara (1997) (Fig. 2). These slight discrepancies are probably related to the incorporation of some amount of taenite (Ni, Pd, and Au; Okabayashi et al., 2019), silicate (Ga), and/or sulfide (Au, Cu) in the fractions analyzed by Kong and Ebihara (1997). Overall, these results are consistent with the range of kamacite compositions reported in H3 chondrites by Campbell and Humayun (2003) (Fig. 2). We did not observe any striking difference between kamacite compositions inside and outside of chondrules (Fig. 2B, C, E, F). Compared to kamacite, taenite in EOCs is enriched in platinum-group elements (PGEs), Au, Cu, Ga, and Ge (Fig. 2D–G).

3.3. Elemental composition of kamacite

Kamacite in UOCs show more grain-to-grain variability (Fig. 2A–C) in both HSE and volatile MSE-chalcophile elements than that in EOCs (Fig. 2D–G). In the most pristine samples Asuka 881236 (H3.1), Sharps (H3.4), and Dhajala (H3.8), Re concentrations vary from 0.070 ± 0.029 to 0.86 ± 0.16 ppm and Os from 0.26 ± 0.48 to 7.1 ± 1.5 ppm; Re/Os ratios (0.026–0.69, Fig. 3A–B) are consistent with the bulk metal Re/Os ratios in these chondrites (Fischer-Gödde et al., 2010) and the previously reported range for kamacite in H3 chondrites (0.065–0.19; Campbell and Humayun, 2003). Tungsten and Mo concentrations range from 0.050 ± 0.040 to 2.10 ± 0.34 ppm and 1.34 ± 0.17 to 319.1 ± 33.9 ppm, respectively. Similar to Kong and Ebihara (1996), our W/Mo ratios are below the OC equilibration line (ratio reached during thermal equilibrium, slope = 0.195, Fig. 3F), due to the incorporation of Mo in sulfides. Iridium concentrations range from 0.460 ± 0.060 to 7.4 ± 2.9 ppm and show a weak positive correlation with Re and stronger positive correlations with Os, Ru (0.210 ± 0.070 to 9.2 ± 1.6 ppm), Pt (0.290 ± 0.010 to 16.8 ± 1.5 ppm), and Rh (0.080 ± 0.030 to 2.48 ± 0.52 ppm) (Fig. 3A–E). The Os/Ir, Ru/Ir, Pt/Ir, and Rh/Ir ratios deviate from the bulk OC ratio at low Ir contents (<2 ppm), but correlate well with the bulk ratios at higher Ir concentrations (Fischer-Gödde et al., 2010) (Fig. 3B–E). We observed relatively constant Pd (1.58 ± 0.37 to 4.2 ± 1.2 ppm) and Au concentrations (0.330 ± 0.090 to 1.090 ± 0.060 ppm) that did not vary with Ir concentration, and Au/Ir and Pd/Ir ratios are not consistent with bulk ratios (Fig. 3G–H). Okabayashi et al. (2019) reported similar observations and linked the constant Au

and Pd concentrations to their diffusion into high-Ni phases. In contrast to the other MVEs, Ge concentrations in UOC kamacite (43.1 ± 2.2 to 75.2 ± 3.2 ppm, with two grains exceeding 80 ppm) vary little from one grain to another and are very similar to the composition of the bulk metal (~ 70 ppm; Kong et al., 1998). This is consistent with the high Ge content of kamacite relative to the bulk metal ($>85\%$ of the Ge in the metal is in kamacite; Goldstein, 1967) and the preferential partitioning of Ge into low-Ni phases in H3 chondrites (Campbell and Humayun, 2003). Similar to Au and Pd, Ge contents do not vary with Ir concentration, leading to Ge/Ir ratios of 14.5–123 in Asuka 88123, 5.2–115.8 in Sharps, and 8.0–81.0 in Dhajala, and a median Ge/Ir ratio of 28 in the studied UOCs (Fig. 4). Of the less siderophile elements, Ga (0.059 ± 0.012 to 42.7 ± 1.8 ppm) is an exception in UOCs and can be either depleted or enriched (Fig. 2) in UOC kamacite compared to the bulk metal. This attests to its ambivalent behavior, which changes from siderophile to lithophile depending on the redox state (Chou and Cohen, 1973). In comparison, Cu in kamacite (10.9 ± 1.1 to 367.2 ± 37.2 ppm; Fig. 2) is always depleted compared to the bulk metal, likely due to its incorporation in sulfide phases.

With increasing metamorphism, we observe an increase and progressive homogenization of total HSE–MSE contents from H3 to H6 (see sup. Mat. Table A3 for full values); *i.e.* from Ste. Marguerite (H4Fig. 2D) to Allegan (H5, Fig. 2E), Guareña and Kernouvé (H6Fig. 2F), and reaching a very homogenous elemental composition in Portales Valley metal veins (H6Fig. 2G). This narrowing of kamacite elemental contents around the mean value of the bulk metal from UOCs to EOCs is consistent with parent-body metamorphism, which tends to homogenize elemental compositions (Gilmour and Herd, 2020). This homogenization results in similar correlations in both EOCs and UOCs for every element except W and Mo (Fig. 3), and elemental ratios approaching the bulk ratio; *e.g.* in H6 chondrites, Ge/Ir ranges from 10 to 35 with a mean of ~ 23 (Fig. 4). In contrast, the W/Mo ratio in EOCs does not tend toward the mean bulk metal value but to an equilibration line (slope = 0.195, Fig. 3F), highlighting Mo incorporation into sulfides phases (Kong and Ebihara, 1996).

4 Discussion

4.1. Processes redistributing moderately volatile elements in H3 chondrites

Processes that redistribute elements between and within chondrites components are multiple (i.e. evaporation, thermal metamorphism, kamacite-taenite formation). Prior to develop a melting model (see next section), their impact onto the elemental composition of kamacite needs to be evaluated.

Evaporation can play a major role in establishing the volatile element contents of metal during the formation of the first solids in primitive materials, and therefore may explain the range of metal compositions observed in H3 chondrites. Metal compositions controlled by evaporation are expected to be depleted in volatile compared to refractory elements. However, our data do not show any marked depletion of Au, Pd, or Ge compared to the bulk metal at a given Ir content (Figs. 3G–I, 4A), precluding the dominance of evaporation in establishing the observed Pd/Ir, Au/Ir, and Ge/Ir ratios in H3 kamacite.

In comparison, progressive parent-body metamorphism from UOCs to EOCs decreased the range of metal compositions (Fig. 3C). Intimately linked with thermal metamorphism, the immiscibility between α Fe-Ni (kamacite) and γ Fe-Ni (taenite) phases is known to redistribute elements by diffusion between high-Ni (>10 wt.%) and low-Ni (<10 wt.%) solid phases (Mullane et al., 2004). HSEs (Mullane et al., 2004; Gilmour and Herd, 2020) and, to a greater extent, MSEs (Okabayashi et al., 2019) are sensitive to this process. Gilmour and Herd (2020) highlighted slight correlations of PGEs, Re, Os, Ir, Ru, and Rh, with Ni with increasing metamorphism from H4 to H6 chondrites but not in pristine H3. In addition, the reported maximum temperature attained during the parent-body metamorphism of type-3 OCs (~ 700 °C; Tait et al., 2014) is too low to trigger the melting of Fe-Ni \pm (S, C) alloy ($T_{\text{solidus}} \approx 1000$ °C). Extensive HSE fractionations by fractional melting after accretion thus seems very unlikely. By comparison, the depleted Pd and Au contents from H3 to H6 compared to the bulk metal (Fig. 2) indicates the redistribution and enrichment of Pd and Au by up to two orders of magnitude in taenite compared to kamacite prior to the accretion, such that, it makes Pd and Au not suitable tracer for metal formation/evolution. In contrast, from figure 2, Ge concentrations in kamacite appear to show systematic changes with respect to petrographic type, being similar to bulk metal in type 3 and 4, but depleted compared to taenite in type 5 and 6, implying that Ge resides largely in kamacite in type 3 and 4 and moves into taenite during higher grade metamorphism. This is consistent with Ge

preferential partitioning into low-Ni phases in H3 chondrites (Campbell and Humayun, 2003). Therefore, the identical Ge content between metal bulk and kamacite in *H3 chondrites* imply that sub-solidus $\alpha\text{Fe-Ni}$ – $\gamma\text{Fe-Ni}$ immiscibility has little impact on Ge partitioning between kamacite and taenite at low petrographic grades (Fig. 4B).

Excluding Au and Pd, PGEs as well as Ge composition of H3 metal phase remains unmodified or only slightly impacted by secondary processes. Then, metal kept the pristine PGE–Ge composition acquired during metal formation or the last step of its evolution. In the following discussion we are using these elements and their relations to discuss pre-accretionary processes.

4.2. Metal melting and crystallization as indicated by the Ge/Ir ratio

Previous models of metal compositional variations in ordinary chondrites were based on the decoupling of HSEs during complex condensation and melting processes (Horan et al., 2009; Okabayashi et al., 2019). However, none of these studies have investigated metal melting and crystallization by combining Ir, Ge, and Au, despite their extensive use to model fractional crystallization during the formation of magmatic iron meteorites (Goldstein et al., 2009). Here, because Au is very sensitive to kamacite–taenite sub-solidus diffusion (Mullane et al., 2004), we use Ge/Ir to investigate the origin as well as melting and crystallization history of UOC metal.

Both Ir and Ge are strongly sensitive to melting and crystallization in Fe-Ni-S and Fe-Ni-C metal compositions. Germanium behaves slightly incompatibly with respect to pure Fe-Ni metal (metal–liquid partition coefficient $D_{\text{Ge}} = 0.63$) and Ir compatibly ($D_{\text{Ir}} = 1.49$; Chabot et al., 2017). With increasing S or C content in the Fe-Ni liquid, D_{Ge} slowly increases with values close to 1 ($D_{\text{Ge}} = 1.5$ at 15% S and 4% C), and Ge becomes compatible with the metal at 5% S and 2% C (Chabot and Jones, 2003; Chabot et al., 2006). In contrast, D_{Ir} quickly increases toward high values ($D_{\text{Ir}} = 10$ at 15% S and 4% C), hence Ge behaves less and less compatible compared to Ir; *e.g.* $D_{\text{Ge}}/D_{\text{Ir}} = 0.4$ at 2% S or 1% C, but 0.2 at 12% S and 0.3 at 3% C, in agreement with the constant Ge content at every Ir (Fig. 3I). Thus, whereas the relation between PGE concentrations and Ge/Ir is proportional to $1/\text{Ir}$ (Fig. 5), accounting for the difference between D_{Ge} and D_{Ir} allows us to more precisely model S and C proportions in the metal phase.

According to metal–liquid partition coefficients (Chabot et al., 2017), Fe-Ni melting and crystallization should produce large Ge/Ir variations, with the first liquid produced having a high Ge/Ir ratio and the first solid subsequently crystallized having low Ge/Ir. The Ge/Ir median value in H3-H6 is 23, approximately corresponds to the metal bulk composition as highlighted by metal veins in Portales Valley (Table 1), It permits to subdivide the metal grain compositions into high-Ge/Ir (>23) and low-Ge/Ir (<23) groups (Figs. 4C, 5) characterized by low and high HSE contents, respectively, allowing to strongly differentiate high- and low-PGE groups as defined by Horan et al. (2009) (Fig. 5).

4.3. Melting and crystallization models

4.3.1. Model parameters

We modeled the effects of melting and crystallization on the metal composition (Figs. 6, 7) using the parameterization of Chabot and Jones (2003) and Chabot et al. (2017) for siderophile element partition coefficients in the Fe-Ni, Fe-Ni-S, and Fe-Ni-C systems (Table 1). In a pure Fe-Ni system, Re, Os, and Ru behave compatibly and Pt, Rh, and Pd incompatibly, although they can behave compatibly if the metal contains carbon or sulfur (Chabot et al., 2017). Based on the behavior of Ge and Ir during Fe-Ni–(S, C) melting or crystallization (see section 4.2), the negative correlations of Re, Os, and Ru vs Ge/Ir (Fig. 5) must be associated with a fractionation between solid and liquid metal phases. Yet, the depletion of Pt, Rh, and Pd in metals with high Ge/Ir (Fig. 5) indicates their compatible behavior. The large range of observed metal compositions must therefore reflect the melting or crystallization of a sulfur- and/or carbon-bearing Fe-Ni metal. Although Okabayashi et al. (2019) reproduced L3 and LL3 OC metal compositions by modeling the crystallization of C-only (0–3.8 wt.%) and S-only (up to 2.3 wt.%) Fe-Ni metals, natural OC metal contains both C and S (Jarosewich, 1990). Understanding HSE variations in a combined Fe-Ni–(S, C) system therefore requires specific parametrization coefficients (Chabot et al., 2017), which we present here.

We calculated the metal–liquid partition coefficient D_E of element E as (Chabot et al., 2017):

$$\ln(D_E) = \ln(D_0) + \beta_{ij} \ln(\text{Fe Domains})$$

where D_0 is the partition coefficient of E in the C- and S-free Fe-Ni system. ‘Fe domains’ is the fraction of free Fe atoms in the liquid metal, calculated for FeS and Fe₃C as (Chabot and Jones, 2003):

$$\text{Fe domains} = \frac{(1 - 2X_S - 4X_C)}{(1 - X_S - 3X_C)}$$

As suggested by Chabot et al. (2017), we calculated the constant β_{ij} for element E and two light elements i and j after Johns and Malvin (1990):

$$\beta_{SC} = \frac{2X_S}{(2X_S + 4X_C)} * \beta_S + \frac{4X_C}{(2X_S + 4X_C)} * \beta_C$$

where β_S and β_C are constants that measure the interaction between element E and S or C, respectively (John and Malvin, 1990), and X_S and X_C are the molar fractions of S and C in the liquid, respectively, which are recalculated at each melting or crystallization step. We used the apparent distribution coefficient of S, k_s , of Haack and Scott (1993) to model the evolution of k_s as the S concentration changed in the liquid, and adopted $k_C = 0.4$, calculated from the experiments of Chabot et al. (2006). All parameters are reported in Table 1. The starting composition was taken as the mean composition of metal grains in H3 chondrites measured herein (Table 1), which are similar to the compositions of melted metal veins in Portales Valley (H6; Figs. 4C, 5). The average carbon content and total Fe content in the UOC metal (assumed present as FeS and Fe⁰; Fe \approx 12.5 wt%, C \approx 0.26 wt% Jarosewich, 1990) were used to estimate the maximum carbon contents of OC metal precursors. By assuming that most carbon in OCs was occurring in the metal, we estimate a maximum of \approx 2 wt.% C in the metal precursors. The occurrence of sulfur within the metal of H, L, and LL chondrites during melting is supported by the high FeS contents in bulk OCs (\sim 5–6 wt.%; Jarosewich, 1990).

4.3.2. Metal crystallization

The fractional crystallization of the metal during cooling of the protoplanetary disk or after heating in the region of OC metal formation can be modeled to assess OC metal grain compositions. We ran Fe-Ni-(S, C) crystallization models with 0–12% S and/or 0–2% C (Fig. 6). Phosphorus has been omitted from this discussion as it does not produce satisfactory results whatever melting/crystallization models or S, C percentages. Models including S or C alone failed to reproduce OC chondrite compositions (Fig.

6); therefore, the fractional crystallization of compositions containing only S or C alone cannot explain the compositional variations observed in H3 metal. Although we cannot exclude the incorporation of HSE-rich refractory particles into the metal (Horan et al., 2009) or Au enrichment in taenite (Okabayashi et al., 2019 and reference therein), several arguments challenge these hypotheses. (1) Compared to Au, Ir is not sensitive to $\alpha\text{Fe-Ni}$ – $\gamma\text{Fe-Ni}$ sub-solidus reactions in type-3 chondrites (Campbell and Humayun, 2003; Okabayashi et al., 2019). Therefore, kamacite should be depleted in Au compared to the crystallization models in the Ir vs Au diagrams (Fig. 6A, C). However, in both diagrams, most metal grains are enriched in Au relative to the crystallization models. (2) Similarly, in type-3 chondrites, the preferential partitioning of Os into kamacite with respect to taenite during $\alpha\text{Fe-Ni}$ – $\gamma\text{Fe-Ni}$ sub-solidus reactions (Campbell and Humayun, 2003) contradicts the depletion of Os in OC metal compared to the crystallization model (Fig. 6E). Additionally, Ir vs Os variations are better fit by the Fe-Ni-S-C crystallization model than the Fe-Ni-C model (Fig. 6F), indicating that the starting material was more likely Fe-Ni-S-C metal than a composition containing only S or C.

4.3.3. Metal melting

We ran melting models using the same parameters as for fractional crystallization (*i.e.* 0–12% S and/or 0–4% C). The best fits were obtained for a starting composition with 1.5 wt.% C and 0–12 wt.% S (Fig. 7A–F). Our models predict the first liquids produced by Fe-Ni-S-C alloy melting to be depleted in HSEs, resulting in a high Ge/Ir ratio, and the first solids to have high HSE contents and Ge/Ir values near those of the starting composition. At higher degrees of melting, the liquid is progressively enriched in HSEs and has a slowly decreasing Ge/Ir ratio, whereas the solid is quickly enriched in HSEs and has a strongly decreasing Ge/Ir ratio, consistent with the HSE concentrations in OC metal phases (Fig. 7A–F).

During partial melting, any small residual metal grains that separate from the melt will be enriched in refractory elements (Re, Os, Ir, Pt, Ru, Rh) compared to the melt due to the compatible behaviors of those elements (Chabot et al., 2017), explaining the effect of grain size on composition (Horan et al., 2009). The compositional diversity of metal grains must then result from various degrees of melting. Moreover, any important compositional variations of the metal precursor can be ruled out in light of the well-constrained HSE contents and the lack of any pronounced vertical deviation from the starting composition in the HSE vs Ge/Ir diagrams (mostly within ~ 1 orders of magnitude; Fig. 7A–F). These results indicate that metal melting was the main process driving the observed compositional ranges. In addition, metal grains that have $\text{Ge/Ir} > 40$

show deviations of refractory elements (*i.e.* for Os, Re, Ru, Pt) from the model curves towards higher HSE contents (*e.g.* Pt content is 2 to 4 ppm higher than modeling curves, Fig. 7). These compositions cannot be reproduced with our melting model, even with unrealistic C or S contents and have to be related to another process. Interestingly, these high anomalous compositions affect only elements with $T_{50\% \text{ condensation}} > \text{Pd}$ and are observed only for the liquid with the lowest HSE content (Fig. 7). It indicates that a small proportion of refractory HSEs were likely incorporated into the liquid metal during melting *via* refractory grains formed at high temperature (Horan et al., 2009).

According to our model, the various metal compositions can be explained at a single carbon content, but require a range of sulfur contents in the starting material, which could be ascribed to two processes. First, a heterogeneous repartitioning of S within metal precursors would imply different starting compositions, which is unlikely given the lack of pronounced vertical variations of the metal composition around the starting composition. Second, some sulfur may have been heterogeneously evaporated from the metal during the heating event(s). However, either of these processes must have occurred at a constant C content, which could be related to the melting temperature of Fe-Ni-S and Fe-Ni-C systems. Indeed, at 1 bar, Fe-Ni-S and Fe-Ni-C alloys respectively melt at 988 °C (Fei et al., 1997) and 1153 °C (Hirayama et al., 1993 and references therein). During metal melting, sulfur, as the most volatile species of these elements, will evaporate from the Fe-Ni-S melt above the eutectic (Tachibana and Huss, 2005), whereas the more refractory carbon will remain dissolved in the metal (*e.g.* Fe₃C; Mikhail and Füre, 2019). Therefore, it is reasonable that the sulfur content in the metal varies from grain to grain depending on the size of the particles before heating and the evaporation-condensation effect at grain edges.

Subliquidus and subsolidus data can be modeled by mixing between liquid and solid phases. As examples of extreme cases, we show specific mixing curves between the last solid composition (after 99% melting) and liquids resulting of 30%, 50%, 70%, and 90% melting in Fig. 7B. Such extreme cases of mixing require efficient liquid–solid segregation, differently sized metal grains, and a dense environment. Nonetheless, they highlight the full range of HSE compositions that can be achieved by mixing solids and liquids formed at different percentages of metal melting, and can account for Os/Ir variations reported by Okabayashi et al. (2019). These various degrees of melting can imply multiple events of partial melting, but the consistency between modeling curves and PGEs data, as well as the uniqueness of the starting composition, suggest metal formation from a homogeneous metallic precursor during one melting event. To be in accordance with the model presented here, this precursor has to be FeNi metal, but the process leading to its elemental homogeneity remains uncertain. This homogeneity and the high contents of PGEs ($\approx 10 \times \text{CI}$, Fig. 2) in the metal cannot be explained by

condensation. Indeed, PGEs condense into refractory alloys, before the metal. So these PGE-alloys are likely to be incorporated randomly in metal phases, as function of Fe-Ni nucleation, creating heterogeneously PGEs-depleted metal phases. A possibility is to produce a homogeneous precursor phase by mixing refractory-alloys and FeNi-metal during a melting stage(s) within a hot and dense environment such as the inner solar system. It implies that H3 chondrites precursors, and then the inner solar system, experienced a sequence of large-scale transient heating-cooling events, such as shock waves (e.g. Connolly and Love, 1998), and that the current metal composition reflects that last heating spike.

The occurrence of both C and S within the Fe-Ni metal, and the fact that metamorphism cannot account for the UOC metal composition, point out that the partial melting of metal precursors occurred before the accretion of the OC parent bodies but after C-S condensation, *i.e.* in a momentarily 'cold' area of the protoplanetary disk. In addition, the depletion of moderately volatile elements in the bulk metal compared to refractory ones (Fig. 2) could reflect metal devolatilization during heating. Nevertheless, the similar condensing temperatures of Cu and Au (*i.e.* $T_{50\%}=1037\text{K}$ and 1060K , respectively) makes Cu volatilization unlikely while keeping Au in the metal phase. Similarly, the lack of evidence for the depletion of volatile Au, Pd, and Ge in kamacite grains (Fig. 3) does not support evaporation process and seems difficult to reconcile with temperature of FeNiS melting ($T_{\text{eutectic}}\approx 1000^\circ\text{C}$ at 1 bar). Hence, preservation of moderately volatile elements in the metal implies heating and cooling timescales shorter than elemental diffusivity. At 988°C , elements of interest (*i.e.* Au, Pd, Ga, Cu, Ge) diffuse at a rate of $D\approx 10^{-15}\text{ m}^2/\text{s}$ (Righter et al. 2005) equivalent to $\approx 10\mu\text{m}/\text{h}$. At an ambient nebular temperature below $T_{50\%\text{condensation S}} (399^\circ\text{C}$, Wood et al. 2019), heating waves of 1000°C that last for 3h or less will not produce significant devolatilization in grains larger than $30\mu\text{m}$ radii. In consequence, we suggest that the melting of the metal precursors resulted from large-scale heating wave(s) with high heating ($>10^3\text{ K/hr}$) and cooling rates ($>10^2\text{ K/hr}$; Tachibana et al., 2006). Regarding OC parent bodies accretion (Desch et al. 2018), the melting event(s) has to occur within 2 Ma after CAIs formation.

4.4. Metal-silicate interactions before accretion

At the grain scale, the distributions of Ga, W, and Mo are more variable compared to those of Re, Os, Ru, Pt, Ir, Pd, and Ge (Fig. 2A–C); for Mo, no clear correlation against Ge/Ir exists (Fig. 5). Chabot et al. (2017) did not report a parametrization for Mo in the Fe-Ni-C system, making it impossible to model Mo variations during melting in the Fe-Ni-S-C system. For Ga and W, only some of the Ga concentrations and almost none of the W compositions can be explained by melting-mixing processes (Fig. 7G–H). In addition, the vertical variations of Ga and W concentrations about the starting compositions (at least ≈ 2 orders of magnitude; Fig. 7G–H) likely indicate various metal precursor compositions, in contrast with the well-defined concentrations of other elements (within ≈ 1 orders of magnitude; Fig. 7A–F).

During the heating event(s) that triggered precursor metal melting, volatilization could have had a major impact on the concentrations of moderately volatile elements. As Ga is less volatile ($T_{50\%} = 1010$ K) than Ge ($T_{50\%} = 830$ K; Wood et al. 2019), elemental variations linked to evaporation will result in the depletion of Ge compared to Ga. However, such a depletion is not observed in OC metal phases (Fig. 3), and volatilization cannot explain the observed Ge/Ir variations (Fig. 4A). This also excludes any significant role of evaporation/volatilization in producing the strong depletion of Ga in the metal.

Rubin (2005) demonstrated that olivine and pyroxene in very primitive UOCs (type 3.0–3.4) show large Fe content variations (*i.e.* fayalite content, Fa, in olivine and ferrosilite content, Fs, in pyroxene) compared to those in EOCs. These variations most likely result from the occurrence of various oxidation states during chondrule formation. Gallium is more sensitive to oxidation state than Ge (Chou and Cohen, 1973); Ga can be siderophile or lithophile during melting depending on its redox state (Wai and Wasson, 1979; Blanchard et al., 2015), such that small redox variations can produce important changes in the Ga content of metal. During metal melting in an oxidizing environment, Ga in the metal is oxidized to GaO and GaOH, and is incorporated into coexisting silicates, decreasing the Ga content in nearby metal phases. The proportion of Ga transferred to the silicate increases with increasing concentrations of O, and S (*i.e.* oxidizing agents) and decrease with increasing C (*i.e.* reducing agent) in the environment (Blanchard et al., 2015) and is therefore highly dependent on local redox conditions.

Similarly, W and Mo are very sensitive to oxidation state during metal melting events because they form multiple species (W_{metal} , WO_2 , WO_3 , WS_2 ; Mo_{metal} , MoO_2 , MoO_3 , MoS_2), resulting in their preferential incorporation into metal, silicate, or sulfide depending on redox conditions, with W being more easily oxidized than Mo (Fegley

and Palme, 1985). When sulfur is present, Mo is more easily sulfurized than W (Fegley and Palme, 1985). Our CI-normalized data on UOC and EOC samples show that Mo is enriched relative to W at all Ge/Ir values in UOCs, but relatively depleted in most EOCs (Fig. 8). This difference reflects the incorporation of Mo into sulfides due to increased sulfurization during metamorphism (Fig. 3F) (Kong and Ebihara, 1996). In contrast, UOC-specific patterns can be related to the influence of oxygen; Kong and Ebihara (1996) attributed the low $(W/Mo)_{CI}$ values in L3 chondrites to melting at high oxygen fugacities (fO_2 ; $\log(fO_2) = 10^{-12}$ – 10^{-11}) compared to the usual disk value of 10^{-17} at ~ 1300 °C (Kong et al., 1997), leading to the incorporation of certain amounts of Mo and W into silicates. However, the lack of strong correlation between W or Mo and Ga implies that W/Mo variations are not solely related to fO_2 conditions. Given the high S content required to reproduce metal-grain HSE compositions (Fig. 7), it is likely that the fS_2 played a significant role in W–Mo fractionation. Therefore, heterogeneous fO_2 and fS_2 conditions during melting must have led to various W/Mo ratios in the metal.

The occurrence of multiple redox environments most likely reflects local variations, wherein mineral precursors locally buffered the redox conditions, rather than nebula-scale variations (Connolly et al., 1994). Indeed, the melting of such an assemblage including metal-silicate precursors, dust, and oxidizing agents can create local (grain-scale) oxidizing environments independent of the solar nebula (Fegley and Palme, 1985). Thus, to account for the observed Ga-W-Mo variations in the metal, we suggest that fO_2 and fS_2 were locally defined by the evaporation of heterogeneously distributed oxidizing components such as C-, O-, and/or H-bearing insoluble organic material (Alexander et al., 2007), and/or hydrated phyllosilicates \pm silicates (Florin et al., 2020).

4.5. Comparison of H–L–LL groups

The H, L, and LL chondrite groups form an oxidation sequence (Florin et al., 2020) characterized by an increase in olivine Fa and a decrease in metal content from H to L to LL (Rubin, 2005). However, in the Urey and Craig diagram (Urey and Craig, 1953), *i.e.* $Fe_{metal} + sulfide$ vs $FeO_{silicate}$, H, L, and LL chondrites do not strictly follow the oxidation path, highlighting a loss of metal from H to LL chondrites. This loss is one of the major features of OC evolution.

Metal in H and L/LL chondrites have identical Re, Os, Ir, Pd, and Au contents (Fig. 9), precluding 'thermo-chemical' processes (*sensu lato*) such as redox gradients or the evaporative loss of Fe as the origin of the loss of metal from OC groups. Mass balance dictates that such processes would produce significant changes in metal HSE concentrations (dilution/enrichment) and fractionations due to the large range of compatibilities and volatilities that characterize these elements. In contrast, Kong and Ebihara (1997) linked the increase of bulk-metal siderophile element contents from H to L to LL chondrites to the accretion of H-chondrite metal earlier, at higher temperature, and under more reducing conditions than L/LL-chondrite metal. However, the indistinguishable Re, Os, Ir, Pd, and Au contents in H–L–LL in our study indicate a common episode of formation for OCs and therefore agree with new computational models of H–L–LL formation based on Ca-Al-rich inclusions (Desch et al., 2018). Additionally, local oxidizing environment described in section 4.4 promotes the co-formation of metal and chondrules as evidenced from Hf-W chronology (Hellmann et al., 2019). Moreover, in our melting model, H OC metal contained up to 1.5 wt.% C, similar to the 2 wt.% C reported by Okabayashi et al. (2019; see their Fig. 8) for L and LL metal. We concluded that the formation environment(s) of H, L, and LL metal grains had very similar thermodynamic conditions, but that the lower C content in H OC metal disagrees with H being more reduced than L and LL. In this case, the well-established evolution of redox conditions from H to L/LL metal is likely related to processes occurring after accretion.

The similarity of OC metal grain compositions thus suggests that they formed under similar conditions from a broadly homogeneous source with a constant Fe/HSE ratio. Thus, the variations of metal abundance and bulk-metal HSE concentrations observed in OCs sequence by Kong and Ebihara (1997) must result from the heterogeneous physical distribution of this batch of relatively homogeneous metal grains within the protoplanetary disk, *i.e.* among OC parent bodies.

Recent studies suggest that the structure of the protoplanetary disk is structured such that an important amount of dust was distributed in the OC formation environment which created heterogeneous pressure gradients (Brasser and Mojzsis, 2020; Izodoro et al., 2021). Such pressure gradients could have concentrated Fe-Ni metal grains in the formation region of H chondrites at the expense of those of L and LL chondrites, necessarily after the heating event(s) to avoid dilution effects. Another possibility is that the distribution of metal grains was affected by increased turbulence in the formation region of L and LL chondrites compared to that of H chondrites due to early instabilities within the inner solar system (Rubin et al., 2005).

5 Conclusions

We performed *in-situ* LA-ICP-MS analyses of highly and moderately siderophile elements (PGE, Ni, Co, Fe, Cu, Ga, Ge) in metal grains in type-3–6 H-group ordinary chondrites. Consistent with previous studies, our results highlight the large variability of elemental compositions within kamacite in unequilibrated ordinary chondrites. This range of composition decreases with increasing metamorphism. Using correlations between Ge/Ir, a tracer of metal melting, and highly siderophile element concentrations (*e.g.* Os, Re, Ru, Pt, Rh), we modeled these compositional variations by the melting of metallic phases containing 1.5 wt.% C and up to 12 wt.% S. In this model, the envelope of metal grain compositions (*i.e.* metal grains depleted in HSE compared to the model) can be explained by the envelope of possible mixtures between solid and liquid metal phases.

Our results also highlight large grain-to-grain variations in Mo, W, and Ga contents in H3 metal grains. Based on these variations, we drew the following conclusions.

(1) Oxidizing processes played a major role during metal formation.

(2) The oxidation state varied locally within metal-silicate precursors, buffered by the heterogeneous distribution of oxidizing agents. The associated preferential incorporation of redox-sensitive W, Mo, and Ga species into metal or silicates produced observed depletions/enrichments in the metal.

The very similar contents and relative abundances of HSE in the metal grains of H, L and LL chondrite implies that their metal formed in the same conditions and from the same precursor. Therefore, we conclude that the different metal contents of the OC groups did not result from metal loss due to chemical processes in the protoplanetary disk, but instead from the physical/mechanical distribution/dispersion of the metal after its formation.

6 Acknowledgments

The authors thank M. Gounelle and the Comité de gestion at the Muséum National d'Histoire Naturelle (Paris), T. McCoy and J. Hoskin at the Smithsonian National Museum of Natural History (Washington, D.C.), A. Nieto Codina at the Museo Nacional de Ciencias Naturales (Madrid), and A. Yamaguchi at the National Institute of Polar Research (Tokyo) for providing the meteorite samples. We gratefully thank V. Debaille as associate editor, as well as two anonymous reviewers for their insightful comments that greatly helped to improve this manuscript. The authors thank R. Dennen for his careful corrections.

7 References

- Alexander, C. M. O'D., Fogel, M., Yabuta, H., & Cody, G. D., 2007. The origin and evolution of chondrites recorded in the elemental and isotopic compositions of their macromolecular organic matter. *Geochimica et Cosmochimica Acta*, 71(17), 4380-4403.
- Alard, O., Lorand, J.-P., Reisberg, L., Bodinier, J.-L., Dautria, J.-M., & O'Reilly, S. Y., 2011. Volatile-rich Metasomatism in Montferrier Xenoliths (Southern France): Implications for the Abundances of Chalcophile and Highly Siderophile Elements in the Subcontinental Mantle. *Journal of Petrology*, 52, 2009–2045.
- Blanchard, I., Badro, J., Siebert, J., & Ryerson, F. J., 2015. Composition of the core from gallium metal–silicate partitioning experiments. *Earth and Planetary Science Letters*, 427, 191-201.
- Brasser, R., & Mojzsis, S. J., 2020. The partitioning of the inner and outer Solar System by a structured protoplanetary disk. *Nature Astronomy*, 4(5), 492-499.
- Brenan, J., & McDonough, W., 2009. Core formation and metal–silicate fractionation of osmium and iridium from gold. *Nature Geoscience* 2, 798–801.

- Campbell, A. J., & Humayun, M., 2003. Formation of metal in Grosvenor Mountains 95551 and comparison to ordinary chondrites. *Geochimica et cosmochimica acta*, 67(13), 2481-2495.
- Chabot, N. L., & Jones, J. H., 2003. The parameterization of solid metal-liquid metal partitioning of siderophile elements. *Meteoritics & Planetary Science*, 38(10), 1425-1436.
- Chabot, N. L., Campbell, A. J., Jones, J. H., Humayun, M., & Lauer Jr, H. V., 2006. The influence of carbon on trace element partitioning behavior. *Geochimica et Cosmochimica Acta*, 70(5), 1322-1335.
- Chabot, N. L., Wollack, E. A., McDonough, W. F., Ash, R. D., & Saslow, S. A., 2017. Experimental determination of partitioning in the Fe-Ni system for applications to modeling meteoritic metals. *Meteoritics & planetary science*, 52(6), 1133-1145.
- Chou, C., and Cohen, J., 1973. Gallium and germanium in the metal and silicates of L- and LL-chondrites. *Geochimica et Cosmochimica Acta*, 37, 315-327.
- Cohen, B. A., & Hewins, R. H., 2004. An experimental study of the formation of metallic iron in chondrules. *Geochimica et cosmochimica acta*, 68(7), 1677-1689.
- Connolly, H. C. Jr., Hewins, R. H., Ash, R. D., Zanda, B., Lofgren, G. E., & Bouché-Denise, M., 1994. Carbon and the formation of reduced chondrules. *Nature*, 371(6493), 136-139.
- Connolly H. C. Jr., Huss, G. R., & Wasserburg, G. J., 2001. On the formation of Fe-Ni metal in Renazzo-like carbonaceous chondrites. *Geochimica et Cosmochimica Acta*, 65(24), 4567-4588.
- Connolly H. C. Jr., and Love S., 1998. The formation of chondrules: Petrologic tests of the shock wave model. *Science*, 280, 62–67.
- Desch, S. J., Kalyaan, A., & Alexander, C. M. O'D., 2018. The effect of Jupiter's formation on the distribution of refractory elements and inclusions in meteorites. *The Astrophysical Journal Supplement Series*, 238(1), 11.

- Fegley Jr, B., & Palme, H., 1985. Evidence for oxidizing conditions in the solar nebula from Mo and W depletions in refractory inclusions in carbonaceous chondrites. *Earth and Planetary Science Letters*, 72(4), 311-326.
- Fei, Y., Bertka, C. M., & Finger, L. W., 1997. High-pressure iron-sulfur compound, Fe₃S₂, and melting relations in the Fe-FeS system. *Science*, 275(5306).
- Fischer-Gödde, M., Becker, H., & Wombacher, F., 2010. Rhodium, gold and other highly siderophile element abundances in chondritic meteorites. *Geochimica et Cosmochimica Acta*, 74(1), 356-379.
- Florin, G., Luais, B., Rushmer, T., & Alard, O., 2020. Influence of redox processes on the germanium isotopic composition of ordinary chondrites. *Geochimica et Cosmochimica Acta*, 269, 270-291.
- Gilmour, C.M., & Herd, C.D.K., 2020. In situ analysis of platinum group elements in equilibrated ordinary chondrite kamacite and taenite. *Meteoritics & Planetary Science*, 55: 679-702.
- Goldstein, J. I., 1967. Distribution of germanium in the metallic phases of some iron meteorites. *Journal of Geophysical Research*, 72(18), 4689– 4696.
- Goldstein, J. I., Scott, E. R. D., & Chabot, N. L., 2009. Iron meteorites: Crystallization, thermal history, parent bodies, and origin. *Geochemistry*, 69(4), 293-325.
- Grossman, J. N., & Wasson, J. T., 1985. The origin and history of the metal and sulfide components of chondrules. *Geochimica et Cosmochimica Acta*, 49(4), 925-939.
- Guignard, J., & Toplis, M.J., 2015. Textural properties of iron-rich phases in H ordinary chondrites and quantitative links to the degree of thermal metamorphism. *Geochimica et Cosmochimica Acta*, 149, 46-63.
- Haack, H., & Scott, E. R., 1993. Chemical fractionations in group IIIAB iron meteorites: Origin by dendritic crystallization of an asteroidal core. *Geochimica et Cosmochimica Acta*, 57(14), 3457-3472.
- Hellmann, J. L., Kruijjer, T. S., Van Orman, J. A., Metzler, K., & Kleine, T., 2019. Hf-W chronology of ordinary chondrites. *Geochimica et Cosmochimica Acta*, 258, 290-309.

- Hewins, R. H., Yu, Y., Zanda, B., & Bourot-Denise, M., 1997. Do nebular fractionations, evaporative losses, or both, influence chondrule compositions?. *Antarctic Meteorite Research*, 10, 275-298.
- Hirayama, Y., Fujii, T., & Kurita, K., 1993. The melting relation of the system, iron and carbon at high pressure and its bearing on the early stage of the Earth. *Geophysical research letters*, 20(19), 2095-2098.
- Horan, M. F., Alexander, C. M. O'D., & Walker, R. J., 2009. Highly siderophile element evidence for early solar system processes in components from ordinary chondrites. *Geochimica et Cosmochimica Acta*, 73(22), 6984-6997.
- Izidoro, A., Dasgupta, R., Raymond, S.N. Deienno, R., Bitsch, B., & Isella, A., 2021. Planetesimal rings as the cause of the Solar System's planetary architecture. *Nature Astronomy*.
- Jarosewich, E. (1990). Chemical analyses of meteorites: A compilation of stony and iron meteorite analyses. *Meteoritics*, 25(4), 323-337.
- Kong, P., & Ebihara, M., 1996. Metal phases of L chondrites: Their formation and evolution in the nebula and in the parent body. *Geochimica et Cosmochimica Acta*, 60(14), 2667-2680.
- Kong, P., & Ebihara, M., 1997. The origin and nebular history of the metal phase of ordinary chondrites. *Geochimica et Cosmochimica Acta*, 61(11), 2317-2329.
- Kong, P., Ebihara, M., & Xie, X., 1998. Reevaluation of formation of metal nodules in ordinary chondrites. *Meteoritics & Planetary Science*, 33(5), 993-998.
- Krot, A. N., Keil, K., Scott, E. R. D., Goodrich, C. A., & Weisberg, M. K., 2014. Classification of meteorites and their genetic relationships. *In Treatise on Geochemistry*. Elsevier. pp. 1–63.
- Lauretta, D. S., Buseck, P. R., & Zega, T. J., 2001. Opaque minerals in the matrix of the Bishunpur (LL3. 1) chondrite: Constraints on the chondrule formation environment. *Geochimica et Cosmochimica Acta*, 65(8), 1337-1353.

- Lodders, K., Palme, H., & Gail, H.-P., 2009. 4.4 Abundances of the elements in the Solar System. In *Solar System*, edited by Trümper J. E. Berlin, Heidelberg: Springer Berlin Heidelberg. pp. 712–770.
- McCoy, T. J., Dickinson, T. L., & Lofgren, G. E., 1999. Partial melting of the Indarch (EH4) meteorite: A textural, chemical, and phase relations view of melting and melt migration. *Meteoritics & Planetary Science*, 34(5), 735-746.
- Mikhail, S., & Füri, E., 2019. On the Origin (s) and Evolution of Earth's Carbon. *Elements*, 15(5), 307-312.
- Mullane, E., Alard, O., Gounelle, M. & Russell, S. S., 2004. Laser ablation ICP-MS study of IIIAB irons and pallasites: constraints on the behaviour of highly siderophile elements during and after planetesimal core formation. *Chemical Geology* 208(1-4): 5-28.
- Newsom, H. E., & Drake, M. J., 1979. The origin of metal clasts in the Bencubbin meteoritic breccia. *Geochimica et Cosmochimica Acta*, 43(5), 689-707.
- Okabayashi, S., Yokoyama, T., Nakanishi, N., & Iwamori, H., 2019. Fractionation of highly siderophile elements in metal grains from unequilibrated ordinary chondrites: Implications for the origin of chondritic metals. *Geochimica et Cosmochimica Acta*, 244, 197-215.
- Palme, H., Lodders, K., Jones, A., 2014. Solar System Abundances of the Elements, in: Davis, A.M. (Ed.), *Treatise on Geochemistry*, 2 ed. Elsevier, Oxford, pp. 41-61.
- Rubin, A. E., 2005. Relationships among intrinsic properties of ordinary chondrites: Oxidation state, bulk chemistry, oxygen-isotopic composition, petrologic type, and chondrule size. *Geochimica et Cosmochimica Acta*, 69(20), 4907-4918.
- Righter, K., Campbell, A. J., & Humayun, M., 2005. Diffusion of trace elements in FeNi metal: Application to zoned metal grains in chondrites. *Geochimica et Cosmochimica Acta*, 69(12), 3145-3158.
- Tachibana, S., & Huss, G. R., 2005. Sulfur isotope composition of putative primary troilite in chondrules from Bishunpur and Semarkona. *Geochimica et Cosmochimica Acta*, 69(12), 3075-3097.

Tachibana, S., Nagahara, H., Mizuno, K., 2006. Constraints on cooling rates of chondrules from metal-troilite assemblages (Abstract #2263). In: *37th Lunar and Planetary Science Conference*, CD-ROM.

Tait, A. W., Tomkins, A. G., Godel, B. M., Wilson, S. A., & Hasalova, P. (2014). Investigation of the H7 ordinary chondrite, Watson 012: Implications for recognition and classification of Type 7 meteorites. *Geochimica et Cosmochimica Acta*, 134, 175-196.

Urey, H.C., Craig, H., 1953. The composition of the stone meteorites and the origin of the meteorites. *Geochimica et Cosmochimica Acta*, 4, 36-82.

Van Schmus, W. R., & Wood, J. A., 1967. A chemical-petrologic classification for the chondritic meteorites. *Geochimica et Cosmochimica Acta*, 31(5), 747-765.

Wai, C. M., & Wasson, J. T., 1979. Nebular condensation of Ga, Ge and Sb and the chemical classification of iron meteorites. *Nature*, 282(5741), 790-793.

Walker, R. J., McDonough, W. F., Honesto, J., Chabot, N. L., McCoy, T. J., Ash, R. D., & Bellucci, J. J., 2008. Modeling fractional crystallization of group IVB iron meteorites. *Geochimica et Cosmochimica Acta*, 72(8), 2198-2216.

Weyrauch, M., Zipfel, J., & Weyer, S., 2019. Origin of metal from CB chondrites in an impact plume—A combined study of Fe and Ni isotope composition and trace element abundances. *Geochimica et Cosmochimica Acta*, 246, 123-137.

Zanda, B., Bourot-Denise, M., Perron, C., & Hewins, R. H., 1994. Origin and metamorphic redistribution of silicon, chromium, and phosphorus in the metal of chondrites. *Science*, 265(5180), 1846-1849.

Declaration of interests

☒ The authors declare that they have no known competing financial interests or personal relationships that could have appeared to influence the work reported in this paper.

☐The authors declare the following financial interests/personal relationships which may be considered as potential competing interests:

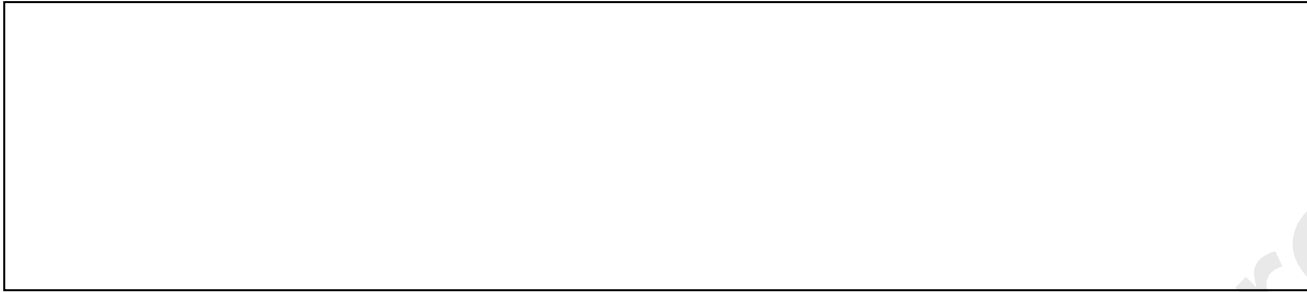


Table 1. Mean elemental compositions of metal grains in each studied meteorite, and partition coefficients (C- and S-free, D_0) and inter-element interaction parameters (β) used to model melting and crystallization. Analytical data are reported in full in the Supplementary Material.

	n	Re pp m	%R SD	Os pp m	%R SD	W pp m	%R SD	Ir pp m	%R SD	Ru pp m	%R SD	M o pp m	%R SD	Pt pp m	%R SD	Rh pp m	%R SD	Ni %	%R SD	C o %	%R SD	Pd pp m	%R SD	A u pp m	%R SD	Cu pp m	%R SD	G a pp m	%R SD	G e pp m	%R SD	Ge/Ir me an m in m ax																																
Kamacite comp.																																																																
Asuka 88123 6	1 4	—	—	2. 3	85	0. 36	91	1. 7	72	2. 4	72	6. 8	60	4. 0	52	0. 61	58	6. 4	13	0. 46	12	2. 3	17	0. 61	29	92 .1	76	4. 4	77	58 .3	11	54. 8	14 .5	12 3																														
Sharps Dhajal a	2 0 1 1	0. 37 0. 29	59	2. 3 2. 6	72 46 78	0. 46 0. 91	57 57 56	2. 2 8	57 57 65	3. 9 4. 2	59 59 24	17 .4 37 .0	92 92 3	6. 5 7. 8	58 58 45	1. 1 1	49 49 23	6. 0 5. 3	14 14 19	0. 38 0. 40	19 19 15	3. 1 0	22 22 20	0. 62 0. 62	29 29 19	11 7 75 .4	60 2 18	4. 2 1. 5	23 6 35	62 .9 58 .6	16 16 7	43. 9 29. 5	5. 3 8. 1	11 6 81 .1																														
Mean H3 ⁽¹⁾		0. 34	61	2. 4	76	0. 56	74	2. 2	66	3. 5	57	18 .9	25 1	6. 0	58	0. 93	50	6. 0	16	0. 41	18	2. 8	24	0. 62	27	99 .1	63	3. 6	18 9	60 .4	13	27. 4																																
Media n H3		0. 30		2. 0		0. 49		2. 2		3. 1		8. 4		5. 5		0. 86		6. 0		0. 42		2. 7		0. 61		86 .6		1. 6		58 .0		28. 1																																
Ste. Margu erite	8	0. 64	91	4. 7	51	1. 2	—	3. 7	49	5. 4	48	7. 5	22	9. 6	30	1. 1	24	9. 6	5	0. 40	18	4. 8	12	0. 80	15	35 5	12	17 .1	6	59 .2	4	23. 1	9. 1	70 .8																														
Allega n	1 0	0. 14	41	2. 4	82	—	—	1. 6	88	2. 5	55	5. 3	18	3. 8	56	0. 47	46	4. 6	38	0. 29	47	2. 5	19	0. 54	9	99 .1	37	8. 8	4	46 .5	5	42. 6	12 .3	71 .6																														
Guare ña	1 4	0. 24	58	3. 4	41	0. 89	20	3. 1	27	3. 7	40	4. 2	42	6. 9	18	1. 1	13	5. 7	10	0. 44	1	2. 2	37	0. 48	43	75 .6	25	10 .7	26	47 .8	23	17. 1	6. 7	33 .5																														
Kernou vé	2	2. 0	12 7	5. 0	90	0. 75	—	2. 2	29	11 .0	85	4. 7	6. 5	27	1. 4	68	4. 3	63	0. 24	11 1	3. 8	31	1. 5	81	23 2	10 9	14 .8	2	55 .1	—	31. 8	—	—																															
Portale s Valey Veins	1 7	0. 33	15	3. 3	8	0. 84	18	2. 8	8	3. 4	8	4. 1	9	5. 8	9	0. 91	6	5. 6	4	0. 50	2	3. 1	15	0. 64	17	18 0	12	15 .8	11	59 .8	5	21. 7	19 .8	26 .9																														
Portale s Valey Clast	4	0. 20	14	1. 8	23	0. 42	51	1. 7	7	2. 3	13	2. 3	46	4. 4	12	0. 64	12	4. 4	3	0. 42	5	1. 2	11	0. 23	12	99 .5	8	7. 4	4	38 .5	4	23. 4	21 .6	25 .2																														
Mean H4- H6 ⁽¹⁾		0. 44	14 6	3. 5	50	0. 82	26	2. 8	42	4. 2	68	4. 9	39	6. 6	37	0. 95	33	6. 2	33	0. 42	26	3. 1	38	0. 65	54	17 6	63	13 .4	28	54 .2	16	19. 3																																
Median H3-H6		0. 40	12 9	2. 9	65	0. 66	56	2. 5	55	3. 8	64	12 .8	28 2	6. 3	49	0. 94	42	6. 1	25	0. 41	22	3. 0	32	0. 63	42	13 4	71	8. 2	90	57 .7	15	23. 3																																
Taenite comp.																																																																
Mean H4-H6		0. 68	86	8. 4	71	0. 77	35	6. 8	72	15 .3	49	9. 0	27	17 .4	73	2. 8	64	38 .0	25	0. 18	33	19 .5	39	2. 4	67	14 68	10 0	49 .6	42	99 .1	42	22. 0																																

<u>Model values</u>																
$D_0^{(2)}$	1. 65	1. 71	0. 95	1. 49	1. 18	0. 67	0. 95	0. 97	–	–	0. 54	0. 37	–	0. 76	0. 63	–
$\beta_c^{(2)}$	0. 27	2. 80	3. 36	4. 23	1. 60	–	4. 81	–	–	–	3. 38	4. 29	–	3. 70	2. 57	–
$\beta_s^{(2)}$	5. 08	5. 34	3. 88	5. 04	3. 89	1. 33	4. 20	2. 66	–	–	0. 71	1. 72	–	2. 81	3. 23	–
Starting composition	0. 34	2. 4	0. 56	2. 2	3. 5	18 .9	6. 0	0. 93	–	–	2. 8	0. 62	–	3. 6	60 .4	27. 4

(1) Ge/Ir ratios are calculated using mean compositions. (2) Data from Chabot et al. (2017) and reference therein. In the melting and crystallization models, Ge/Ir is recalculated at each step based on the Ge and Ir compositions. “–” Not analyzed or data not available. n is the number of grains on which means are based

Figure captions

Figure 1: Reflected-light optical microscope images of the studied ordinary chondrites: (A, B) Sharps (H3.4); (C, D) Dhajala (H3.8); (E, F) Ste. Marguerite (H4); (G) Allegan (H5); (H) Kernouvé (H6); (I, J) Guareña (H6). In all pictures, silicates are dark gray, Fe-Ni alloy is white, and troilite is yellowish-brown.

Figure 2: Spider diagrams of (A–C) H3, (D) H4, (E) H5, and (F, G) H6 chondrites; elements are ordered by increasing volatility. The dark blue line with white symbols is the mean kamacite composition for each sample. The gray shaded area is the range of compositions obtained from LA-ICP-MS analyses of Tieschitz (H3.6; Campbell and Humayun, 2003). The dark gray curve is the bulk metal composition from Kong and Ebihara (1997). Values are normalized to CI chondrites (Lodders et al., 2009). In (F), one grain has a low Ge content of 22.4 ± 1.8 ppm ($\text{Ge}_{\text{CI}} = 0.68$).

Figure 3: Elemental compositions of kamacite in UOCs (blue circles) and EOCs (dark crosses). Black lines in (A–E, G, H) are bulk ratios from Fischer-Gödde et al. (2010), the dashed line in (F) is the W/Mo equilibration line during metamorphism from Kong and Ebihara (1996), and the dashed line in (I) is the bulk metal ratio calculated by linear regression of the H, L, and LL bulk metal data from Kong and Ebihara (1996). The red shaded area is the range of taenite compositions measured in EOCs (this study). Elements are ordered from Re to Ge by decreasing siderophile behavior.

Figure 4: Ge/Ir vs. (A) Ge and (B) Ni contents of kamacite in the studied H3 chondrites. (C) Variation of Ge/Ir in kamacite from the most pristine to the most metamorphosed sample studied here. The dashed line represents the median Ge/Ir composition in all groups.

Figure 5: Siderophile element concentrations vs. Ge/Ir ratio in kamacite. The black dashed line represents the median Ge/Ir ratio across all meteorites studied. UOCs are shown in various shades of blue, and EOCs in other colors. Elements are ordered by decreasing siderophile behavior.

Figure 6: Fractional crystallization models for various metal compositions: (A, B) Fe-Ni-S metal containing 0–12 wt. % S, (C, D) Fe-Ni-C metal containing 0–2 wt. % C, and (E) Fe-Ni-S-C metal containing 0–12 wt. % S and 1.5 wt. % C. (F) Ir vs. Os diagram showing the difference between a S-free melt containing 1.5 wt. % C and a melt containing 12 wt. % S and 1.5 wt. % C; dashed and solid lines are melting ('Melt.') and crystallization ('Cryst.') models, respectively. Red and green lines indicate the solid and liquid compositions, respectively. Only UOC data are shown because EOCs have been modified by parent-body metamorphism and do not represent pristine metal compositions. Blue diamonds are our data and gray circles are from Okabayashi et al. (2019). Percentages refer to sulfur (A, B, E) and carbon (C, D) contents in the starting material.

Figure 7: Elemental analyses of H3 kamacite (blue circles) compared to our batch metal melting model (0.1% melting increments) for Os, Re, Ru, Pt, Pd, W, and Ga vs. Ge/Ir in logarithmic space. Our melting model uses the parametrization of Chabot et al. (2017) for a Fe-Ni-S-C metal containing 1.5 wt. % C and 0–12 wt. % S. Percentages in all panels except (B) refer to the S content of the metal. Red and green lines show the evolution of the solid and liquid compositions, respectively. Dashed lines represent mixing between the residual solid after 99% fusion and a liquid created by 30% fusion. (B) is identical to (A) but highlights various mixing curves between the residual solid after 99% fusion and liquids created by 30%, 50%, 70%, and 90% fusion. Each gray circle along the mixing curves represents a 5% increment, and the Ge/Ir ratio was recalculated using the Ge and Ir concentrations in the liquid at each melting increment. Shaded gray areas incorporate all compositions achievable under these

mixing conditions. Molybdenum and Ru are omitted because no β factors have been reported for melting with C and S.

Figure 8: W/Mo normalized to chondrite plotted against Ge/Ir. The dashed line at $W/Mo_{Cl} = 1$ highlights the upper limit at which W_{Cl} becomes enriched relative to Mo_{Cl} .

Figure 9: Concentrations of refractory (Re, Os, Ir, Pt) and moderately volatile (Au, Pd) siderophile elements in the metal in H (this study) and L/LL chondrites (Okabayashi et al., 2019).

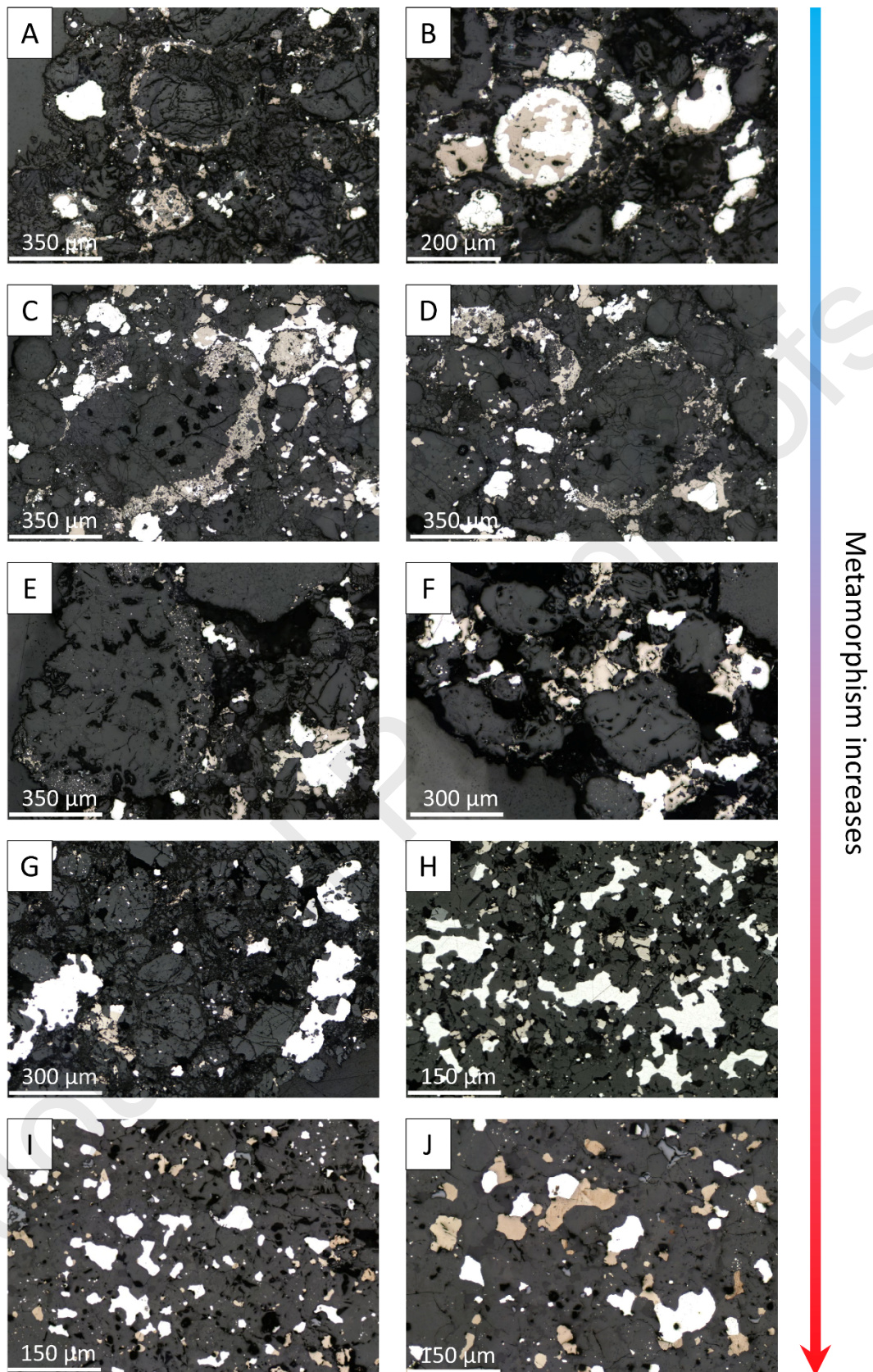


Figure 1, Florin et al. (2022)

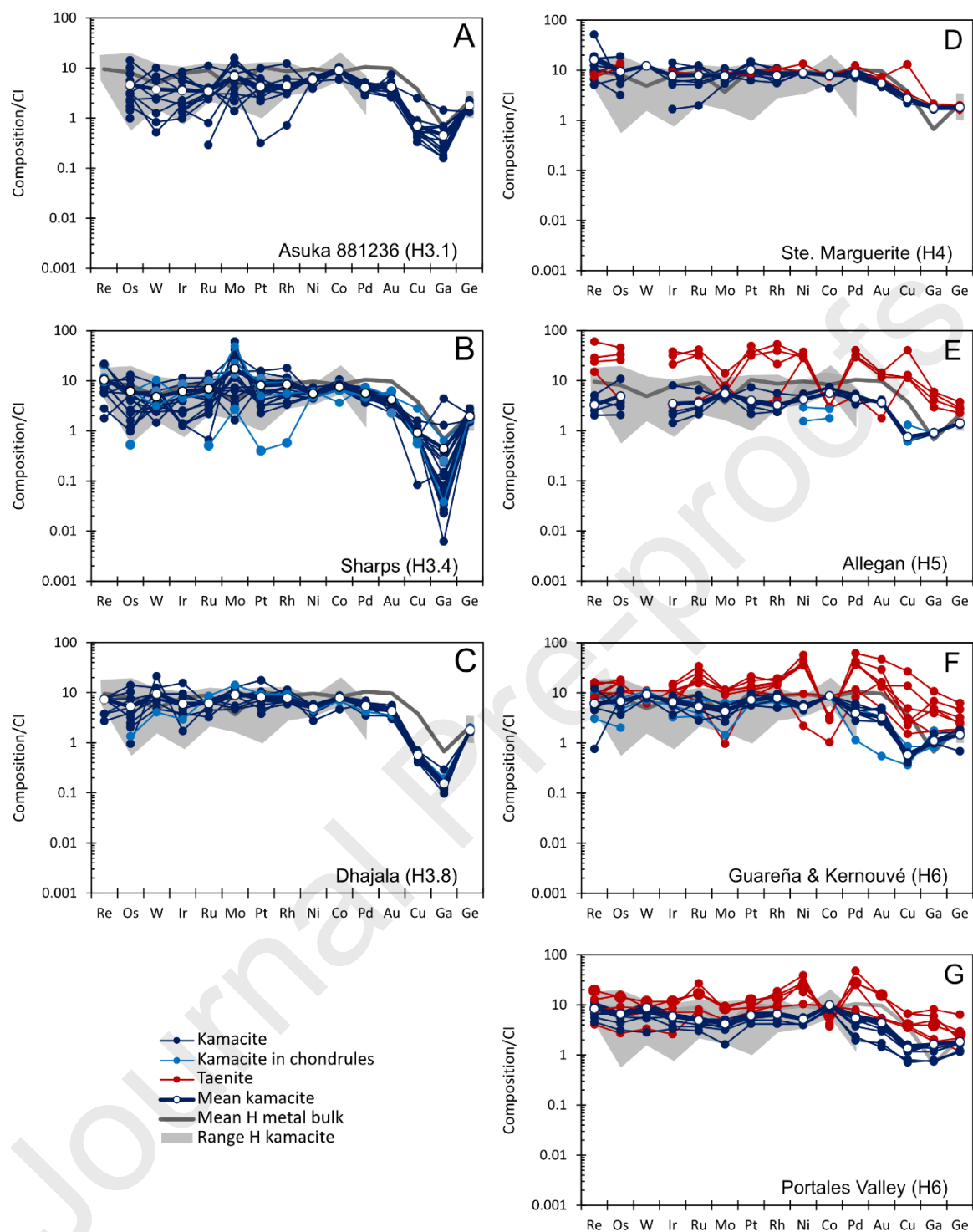


Figure 2, Florin et al. (2022)

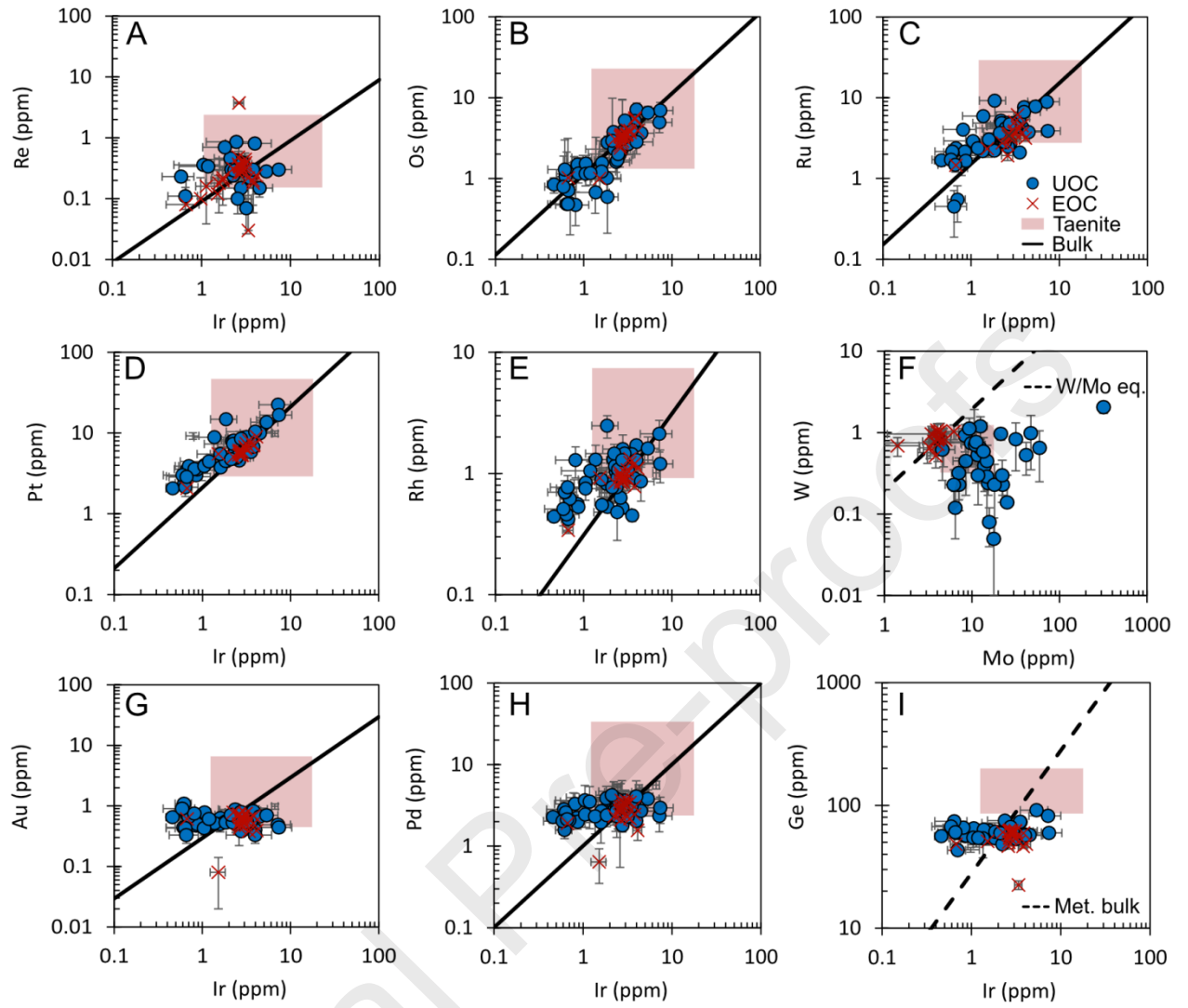


Figure 3, Florin et al. (2022)

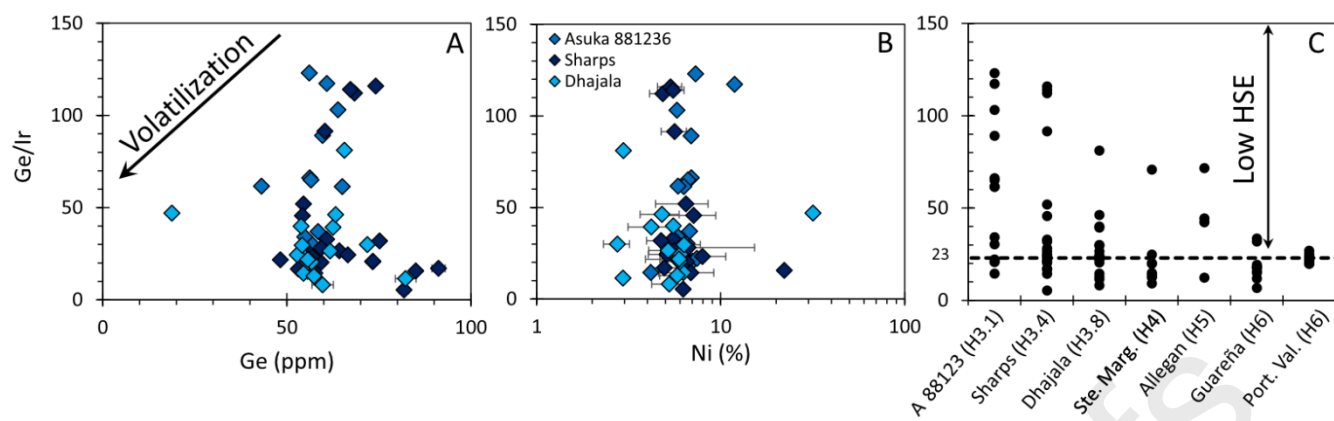


Figure 4, Florin et al. (2022)

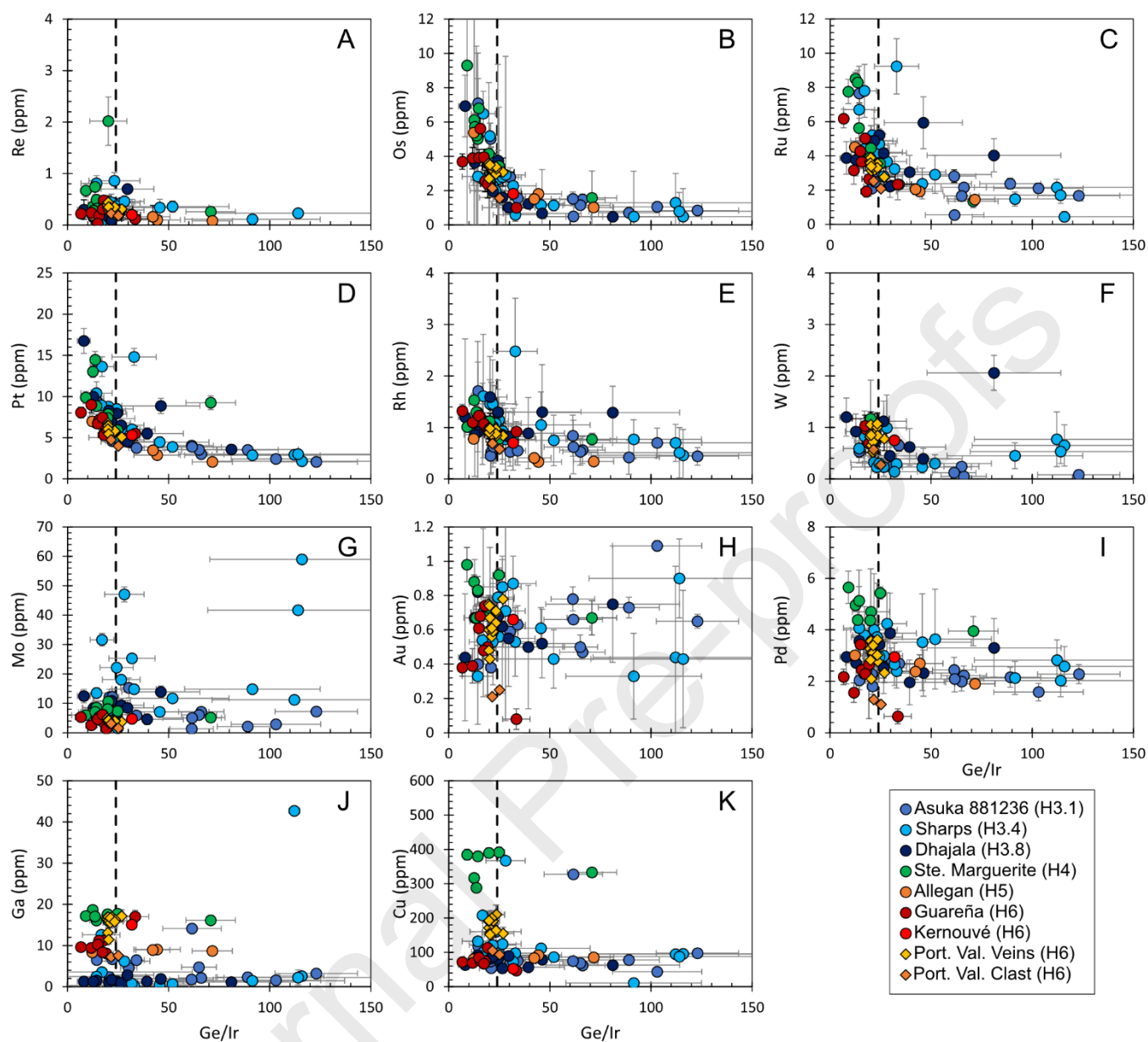


Figure 5, Florin et al. (2022)

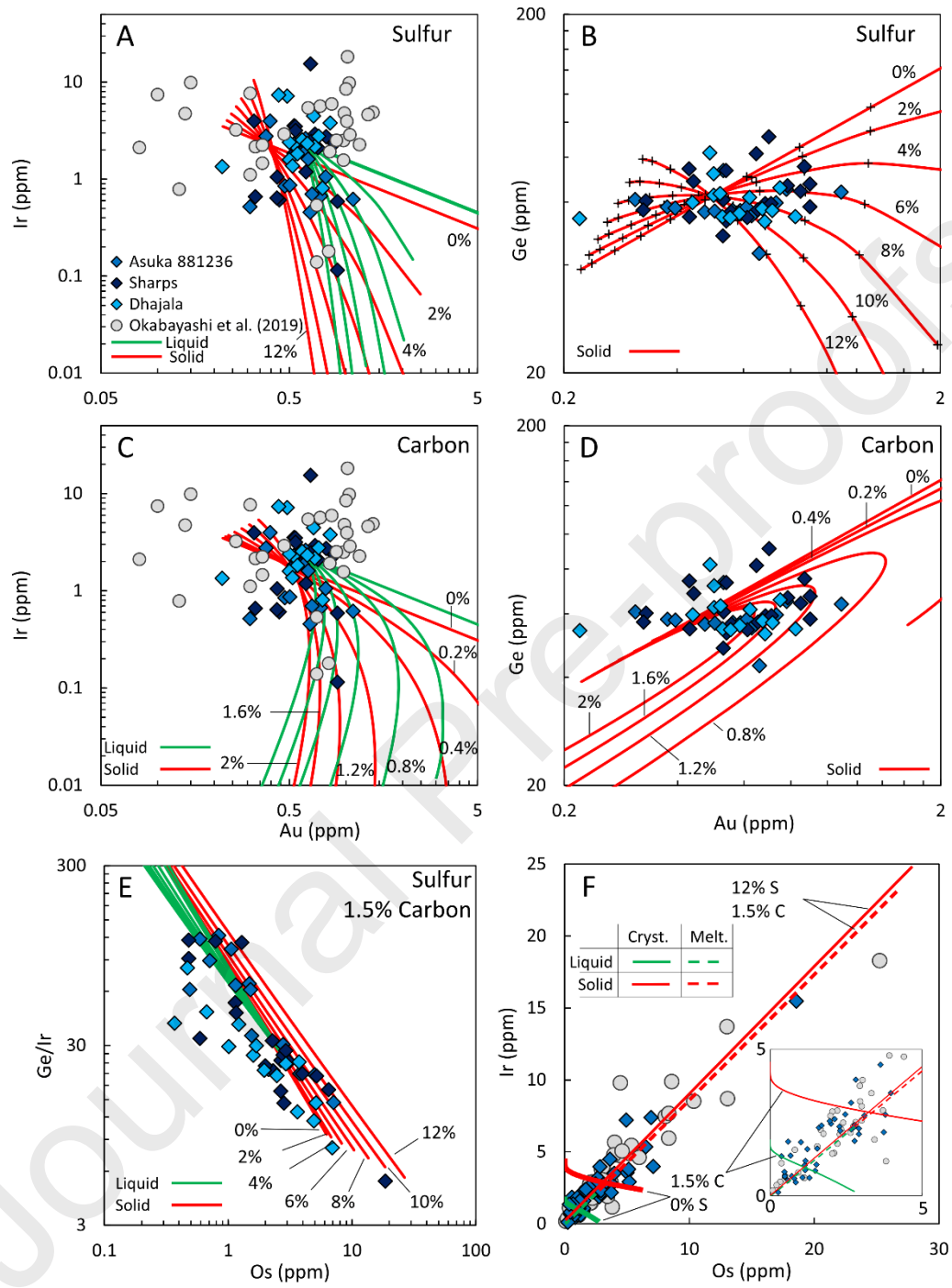


Figure 6, Florin et al., (2022)

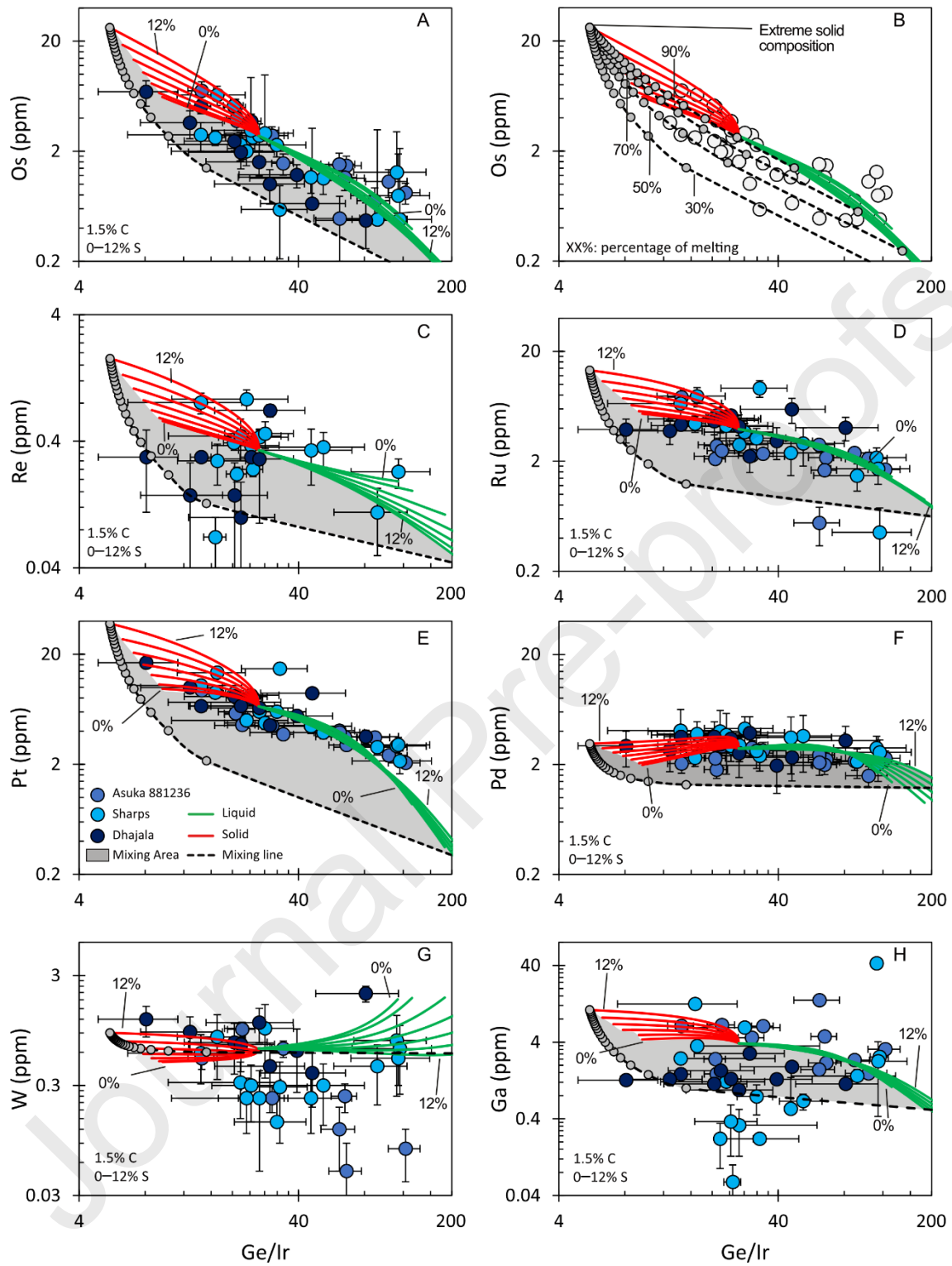


Figure 7. Florin et al. (2022)

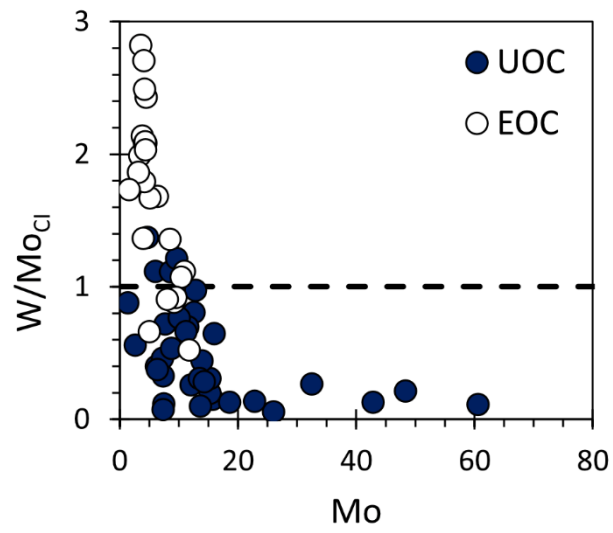


Figure 8, Florin et al. (2022)

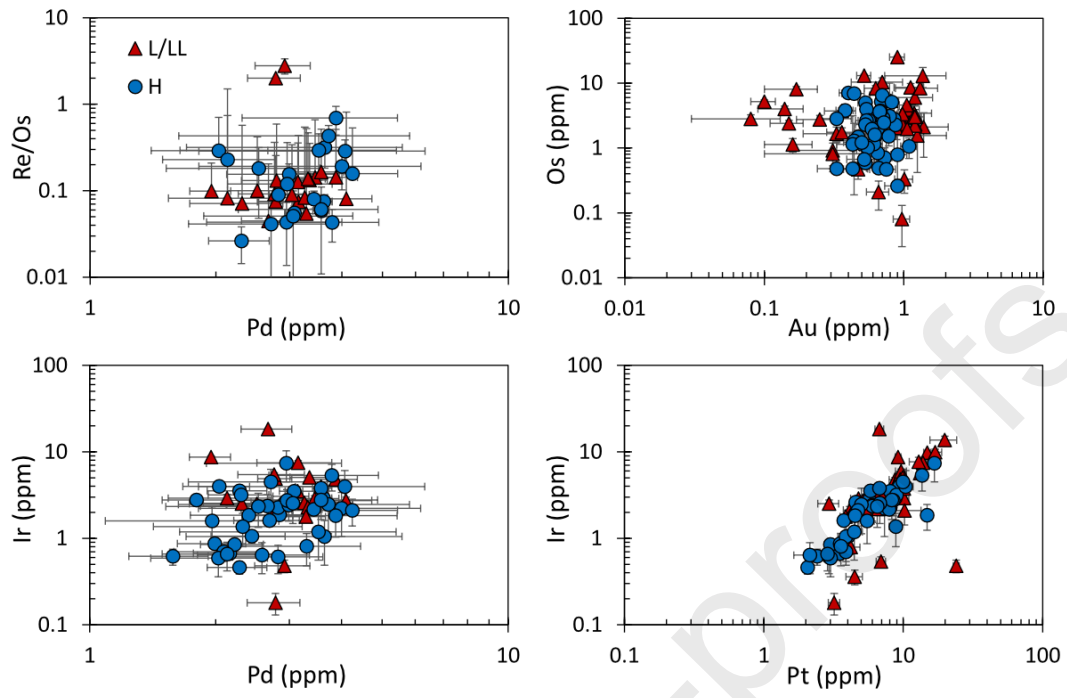


Figure 9, Florin et al. (2022)